Research Square

Preprints are preliminary reports that have not undergone peer review.
They should not be considered conclusive, used to inform clinical practice,
or referenced by the media as validated information.

Efficient Nonlinear Normal Mode Analysis of Wing–Control Surface Structures with Free-Play Nonlinearity Using a CMS–HCF Framework

Chin-Yi Chang
National Tsing Hua University
Meng-Hsuan Tien
mhtien@pme.nthu.edu.tw

National Tsing Hua University

Research Article

Keywords: nonlinear normal mode, reduced-order modeling, free-play nonlinearity, aircraft control surface, numerical method

Posted Date: November 12th, 2026

DOI: https://doi.org/10.21203/rs.3.rs-11426157/v1

License: This work is licensed under a Creative Commons Attribution 4.0 International License.
Read Full License

Additional Declarations: No competing interests reported.

Efficient Nonlinear Normal Mode Analysis of Wing–Control Surface Structures with Free-Play Nonlinearity Using a CMS–HCF Framework

Chin-Yi Chang and Meng-Hsuan Tien*

National Tsing Hua University, Hsinchu 30013, Taiwan
Corresponding author: mhtien@pme.nthu.edu.tw

Abstract. Structural nonlinearities in aircraft control surfaces can significantly influence their dynamic characteristics and aeroelastic behavior. While low-order lumped-parameter models with two or three degrees of freedom have been extensively studied, analyzing nonlinear normal modes (NNMs) of wing–control surface systems using high-dimensional finite element (FE) models remains computationally challenging. Although conventional numerical continuation frameworks (NCFs) have been developed for analyzing NNMs of nonlinear structures, their computational cost increases substantially as the number of degrees of freedom grows. To overcome this limitation, this study presents an efficient computational framework that integrates the Craig–Bampton component mode synthesis (CMS) method with a hybrid continuation framework (HCF) for computing the NNMs of a wing–control surface structure with both structural flexibility and free-play nonlinearity. The HCF is extended and integrated with CMS, and the resulting CMS–HCF framework is then applied to analyze the NNMs of a FE model of an aircraft wing with a control surface. The results show that the frequency–energy curves obtained using the proposed framework exhibit excellent agreement with those computed using the conventional NCF, while achieving computational speedups of approximately 16–36 times. Comparisons with full-order FE simulations further demonstrate that the reduced-order model captures the dominant nonlinear modal characteristics. Furthermore, the analysis of internal resonances reveals modal coupling between the first and second NNM families in the presence of free-play nonlinearity. The effects of both the free-play angle and central stiffness on the NNMs are also investigated using the proposed framework. Reducing the free-play angle shifts nonlinear modal interactions toward lower energy levels, whereas reducing the central stiffness alters the modal-frequency relationship and consequently the order of internal resonance.

Keywords: nonlinear normal mode, reduced-order modeling, free-play nonlinearity, aircraft control surface, numerical method

1 Introduction

The dynamic behavior of aircraft control surfaces is often influenced by structural nonlinearities, which can significantly affect aeroelastic stability [1, 2]. Such nonlinearities may arise from various sources, including free-play, friction, and nonlinear stiffness [3, 4]. Among these, free-play nonlinearity, typically resulting from mechanical clearances in control surface joints, has received particular attention in the literature [5]. Prior studies have demonstrated that free-play can induce limit cycle oscillations [6], alter resonance frequencies [7, 8], and in severe cases, promote flutter [9] or accelerate material fatigue [10]. Although aeroelastic analysis has traditionally relied on linear stability theory, such linearized approaches are often insufficient, as they may neglect essential dynamic characteristics introduced by the structural nonlinearities.

To address the limitations of linear analysis, several researchers have employed nonlinear modeling techniques to investigate the aeroelastic behavior of control surfaces. For instance, Conner [11] investigated the nonlinear aeroelastic response of an airfoil with a control surface using a three degree-of-freedom (DOF) model supported by numerical simulations and wind tunnel experiments. Similarly, O'Neil and Strganac [12] examined the dynamics of a rigid wing equipped with cubic nonlinear springs, revealing the emergence of limit cycle oscillations and bifurcation phenomena. Although these studies successfully highlighted the effects of structural nonlinearity on wing dynamics, they relied on simplified low-order models with only a few DOFs, which limited their ability to capture the structural flexibility of realistic wing structures. To improve physical fidelity, subsequent research has adopted more detailed structural models. For example, Riso and Cesnik [13] employed a full-wing model incorporating geometric nonlinearities associated with large deflections, enabling a more accurate representation of wing aeroelastic dynamics. However, their analysis did not address piecewise-linear nonlinearities such as control surface free-play. Despite these advances in nonlinear aeroelastic modeling, the systematic analysis of the modal properties of high-dimensional wing–control surface systems with localized free-play nonlinearities remains a challenging task.

In nonlinear structural dynamics, the modal characteristics of nonlinear systems can be described through the concept of nonlinear normal modes (NNMs) [14], which provide a fundamental framework for understanding nonlinear vibration behavior. NNM analysis has been extensively applied in structural dynamics; for example, Kuether and Allen [15] developed a numerical methodology for computing NNMs of geometrically nonlinear structures. However, most existing NNM computation techniques rely on iterative numerical procedures that are computationally demanding. As a result, applying NNM analysis to high-dimensional finite element (FE) models remains computationally challenging. To improve the computational efficiency of NNM analysis for complex structural systems, several approaches have been developed. For instance, Peeters et al. [16] developed a computational framework that combines component mode synthesis (CMS) [17] with a numerical continuation framework (NCF) [18], enabling the investigation of modal properties in full-scale aircraft structures. Huang and Tien [19] developed the Hybrid Continuation Framework (HCF) for analyzing NNMs of piecewise-linear systems by integrating the Hybrid Symbolic-Numerical Computational

(HSNC) [20] method with the shooting method and pseudo-arclength continuation. More recently, Chen and Tien [21] proposed a mode selection criterion for the CMS method to further reduce the computational cost of NNM analysis. Although these developments have significantly improved the efficiency of NNM analysis for nonlinear structures, their application to high-dimensional FE models of aircraft wing–control surface structures incorporating both structural flexibility and free-play nonlinearity has not yet been systematically investigated.

In this work, we develop an efficient computational framework for analyzing the NNMs of an aircraft wing–control surface structure modeled using an FE formulation that captures both structural flexibility and free-play nonlinearity. The proposed framework integrates the HCF with CMS to enable efficient NNM analysis of a high-dimensional wing–control surface FE model with localized free-play nonlinearity. In this approach, the Craig–Bampton CMS method is first applied to construct a reduced-order model of the wing–control surface structure. The free-play nonlinearity is represented using a piecewise-linear stiffness element at the hinge DOF connecting the wing and control surface. The HCF is then adapted to compute the NNMs of the resulting reduced-order model. The proposed CMS–HCF framework enables efficient investigation of the nonlinear modal characteristics of wing–control surface structures that exhibit both structural flexibility and free-play nonlinearity. The numerical results obtained using the proposed framework are validated against those computed using the conventional NCF and compared with full-order FE transient simulations, and the computational efficiency of the proposed method is demonstrated. In addition, the nonlinear modal properties of the system, including internal resonance phenomena observed in the wing–control surface structure, are investigated through parametric studies of the free-play angle and central stiffness.

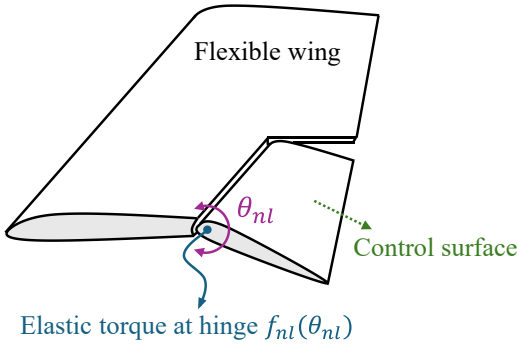
The remainder of this paper is organized as follows. Section 2 introduces the proposed computational framework for NNM analysis. Section 3 presents and discusses the results obtained from the wing–control surface model. Finally, Section 4 summarizes the main conclusions and outlines directions for future work.

2 Methodology

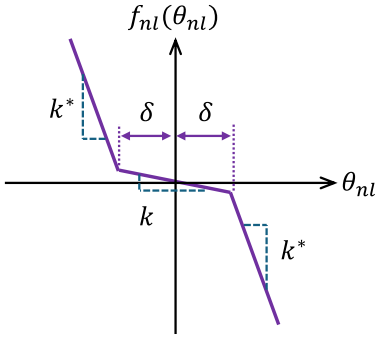
In this section, the original HCF is modified and extended for integration with CMS, enabling efficient NNM analysis of wing-control surface structures. First, the modeling of the piecewise-linear free-play nonlinearity at the control surface hinge, along with the CMS-based reduced-order modeling approach for the wing-control surface structure, is presented. Next, the proposed CMS-HCF framework is introduced.

2.1 Free-Play Nonlinearity in the Control Surface and Reduced-Order Modeling

An aircraft wing with a hinged control surface is schematically illustrated in Fig. 1(a). The rotational motion of the control surface is typically governed by a servo actuator. However, due to unavoidable manufacturing and assembly tolerances, the hinge often exhibits free-play nonlinearity, as depicted in Fig. 1(b). In this study, θ_{nl} denotes the



(a)



(b)

Fig. 1. (a) Aircraft wing–control surface structure. (b) Piecewise-linear restoring torque characteristic of the control surface hinge.

nonlinear DOF representing the rotational angle of the control surface at the hinge, and $f_n(\theta_{nl})$ represents the corresponding elastic restoring torque associated with this nonlinear DOF. The parameter δ denotes the free-play angle. Within the free-play region, the stiffness is denoted by k, while outside this region the stiffness is represented by k^*, where typically $k^* \gg k$. In many previous studies [22, 23], the central stiffness k is assumed to be approximately zero to represent a stiffness-free region within the free-play angle. Accordingly, the restoring torque at the hinge can be expressed as a piecewise-linear function:

$$f_{nl}(\theta_{nl}) = \begin{cases} -k^*\theta_{nl} + f_g, & \theta_{nl} > \delta \ \ (i = 1) \\ -k\theta_{nl}, & -\delta < \theta_{nl} < \delta \ \ (i = 2) \\ -k^*\theta_{nl} - f_g, & \theta_{nl} < -\delta \ \ (i = 3) \end{cases} \tag{1}$$

where $f_g = (k^* - k)\delta$ represents the torque offset required to maintain continuity of the restoring torque at the free-play boundaries. Eq. (1) characterizes the three linear regimes of the system (i.e., $i = 1,2,3$).

Next, to capture the structural flexibility of the wing-control surface system, the entire structure is modeled using the FE method. The equation of motion of the system can be expressed as

$$\mathbf{M}\ddot{\mathbf{x}} + \mathbf{C}\dot{\mathbf{x}} + \mathbf{K}\mathbf{x} = \mathbf{f}_{nl}(\theta_{nl}), \tag{2}$$

where $\mathbf{M}$, $\mathbf{C}$, and $\mathbf{K}$ denote the mass, damping, and stiffness matrices, respectively, and $\mathbf{f}_{nl}(\theta_{nl})$ represents the nonlinear restoring force vector. The coordinate vector is defined as $\mathbf{x} = [\theta_{nl}, \mathbf{x}_l^T]^T$, where $\mathbf{x}_l$ denotes the linear DOFs that are not associated with the nonlinear restoring forces or torques. Accordingly, the nonlinear force vector can be written as $\mathbf{f}_{nl} = [f_{nl}(\theta_{nl}), \mathbf{0}^T]^T$, where $\mathbf{0}$ is a zere vector correspondting to the linear DOFs. In this study, damping is neglected because the primary objective is to analyze the undamped NNMs of the wing-control surface system. By neglecting the damping matrix $\mathbf{C}$, Eq. (2) can be partitioned into block-matrix form as follows:

$$\begin{bmatrix} m_{nl,nl} & \mathbf{M}_{nl,l} \\ \mathbf{M}_{l,nl} & \mathbf{M}_{l,l} \end{bmatrix} \begin{Bmatrix} \ddot{\theta}_{nl} \\ \ddot{\mathbf{x}}_l \end{Bmatrix} + \begin{bmatrix} 0 & \mathbf{K}_{nl,l} \\ \mathbf{K}_{l,nl} & \mathbf{K}_{l,l} \end{bmatrix} \begin{Bmatrix} \theta_{nl} \\ \mathbf{x}_l \end{Bmatrix} = \begin{Bmatrix} f_{nl}(\theta_{nl}) \\ \mathbf{0} \end{Bmatrix}, \tag{3}$$

where the subscripts l and nl denote the linear and nonlinear components of the system, respectively.

Eq. (3) is subsequently reduced using the Craig–Bampton CMS method [24], while retaining the nonlinear DOF θ_{nl} as an active coordinate in the reduction process. The constraint mode $\boldsymbol{\varphi}_c$ is obtained by applying a unit displacement at the nonlinear DOF, resulting in the corresponding static deformation of the linear DOFs. Accordingly, the constraint mode can be expressed as

$$\boldsymbol{\varphi}_c = -\mathbf{K}_{l,l}^{-1}\mathbf{K}_{l,nl}. \tag{4}$$

The fixed-interface normal modes, $\boldsymbol{\Phi}_n$, correspond to the mode shapes of the system with the nonlinear DOF held fixed. These modes are obtained by solving the following eigenvalue problem:

$$\left(\mathbf{K}_{l,l} - \omega^2\mathbf{M}_{l,l}\right)\boldsymbol{\Phi}_n = \mathbf{0}. \tag{5}$$

The CMS transformation matrix $\boldsymbol{\alpha}$ is constructed using the constraint mode and the fixed-interface normal modes as follows:

$$\boldsymbol{\alpha} = \begin{bmatrix} \mathbf{I} & \mathbf{0} \\ \boldsymbol{\varphi}_c & \boldsymbol{\Phi}_n \end{bmatrix}. \tag{6}$$

Only a subset of the fixed-interface normal modes is retained in $\boldsymbol{\Phi}_n$ to reduce the dimensionality of the reduced-order model. Finally, by applying the CMS transformation $\mathbf{x} = \boldsymbol{\alpha}\mathbf{q}$ to Eq. (2), the reduced-order model is obtained as

$$\mathbf{M}_{ROM}\ddot{\mathbf{q}} + \mathbf{K}_{ROM}\mathbf{q} = \hat{\mathbf{f}}_{nl}(\mathbf{q}), \tag{7}$$

where $\mathbf{M}_{ROM} = \boldsymbol{\alpha}^T\mathbf{M}\boldsymbol{\alpha}$, $\mathbf{K}_{ROM} = \boldsymbol{\alpha}^T\mathbf{K}\boldsymbol{\alpha}$, and $\hat{\mathbf{f}}_{nl} = \boldsymbol{\alpha}^T\mathbf{f}_{nl}$. The reduced coordinate vector can be expressed as $\mathbf{q} = [\theta_{nl};\ \boldsymbol{\eta}^T]^T$, where $\boldsymbol{\eta}$ denotes the modal coordinates associated with the fixed-interface normal modes $\boldsymbol{\Phi}_n$. The reduced nonlinear force vector can be written as $\hat{\mathbf{f}}_{nl}(\mathbf{q}) = [f_{nl}(\theta_{nl});\ \mathbf{0}^T]^T$. Thus, the nonlinear restoring torque f_{nl} is retained explicitly in the reduced-order model.

2.2 Combined Component Mode Synthesis – Hybrid Continuation Framework (CMS-HCF)

The HCF is extended and integrated with the CMS model to enable efficient NNM analysis of the wing-control surface structure with free-play nonlinearity. To facilitate this integration, Eq. (7) is reformulated into three sets of linear equations with constant forcing terms. Specifically, the linear components of the nonlinear restoring torque force $f_{nl}(\theta_{nl})$ (i.e., $-k^*\theta_{nl}$ and $-k\theta_{nl}$ in Eq. (1)), are moved to the left-hand side of Eq. (7). As a result, the equations of motion in the three linear regimes can be expressed as

$$\mathbf{M}_{ROM}\ddot{\mathbf{q}} + \overline{\mathbf{K}}_{ROM,i}\mathbf{q} = \hat{\mathbf{f}}_{g,i}. \quad \text{for } i = 1,2,3 \tag{8}$$

The modified stiffness matrices $\overline{\mathbf{K}}_{ROM,i}$ are expressed as

$$\begin{aligned} \overline{\mathbf{K}}_{ROM,1} = \overline{\mathbf{K}}_{ROM,3} &= \begin{bmatrix} k^* & \mathbf{K}_{nl,l} \\ \mathbf{K}_{l,nl} & \mathbf{K}_{l,l} \end{bmatrix}, \\ \overline{\mathbf{K}}_{ROM,2} &= \begin{bmatrix} k & \mathbf{K}_{nl,l} \\ \mathbf{K}_{l,nl} & \mathbf{K}_{l,l} \end{bmatrix}, \end{aligned} \tag{9}$$

and the constant force vectors $\hat{\mathbf{f}}_{g,i}$ are

$$\hat{\mathbf{f}}_{g,1} = \begin{bmatrix} f_g \\ \mathbf{0} \end{bmatrix}, \hat{\mathbf{f}}_{g,2} = \mathbf{0}, \hat{\mathbf{f}}_{g,3} = \begin{bmatrix} -f_g \\ \mathbf{0} \end{bmatrix}. \tag{10}$$

Each set of linear differential equations ($i = 1,2,3$) in Eq. (8) describes the system dynamics within a corresponding linear regime. To eliminate the constant force vector on the right-hand side, a coordinate transformation $\mathbf{q} = \tilde{\mathbf{q}}_i + \boldsymbol{\beta}_i$ is introduced for each regime, where $\boldsymbol{\beta}_i = \overline{\mathbf{K}}_{ROM,i}^{-1}\hat{\mathbf{f}}_{g,i}$. Substituting this transformation into Eq. (8) yields the homogeneous form

$$\mathbf{M}_{ROM}\ddot{\tilde{\mathbf{q}}}_i + \overline{\mathbf{K}}_{ROM,i}\tilde{\mathbf{q}}_i = \mathbf{0}, \tag{11}$$

Next, a modal transformation is applied to decompose Eq. (11) using $\tilde{\mathbf{q}}_i = \boldsymbol{\Psi}_i\tilde{\mathbf{u}}_i$, leading to

$$\boldsymbol{\Psi}_i^{\mathrm{T}}\mathbf{M}_{ROM}\boldsymbol{\Psi}_i\ddot{\tilde{\mathbf{u}}}_i + \boldsymbol{\Psi}_i^{\mathrm{T}}\overline{\mathbf{K}}_{ROM,i}\boldsymbol{\Psi}_i\tilde{\mathbf{u}}_i = \mathbf{0}, \tag{12}$$

where $\boldsymbol{\Psi}_i$ denotes the mass-normalized modal matrix of the system in its i^{th} linear regime, and $\tilde{\mathbf{u}}_i$ represents the associated modal coordinates. With mass-normalized mode shapes, Eq. (12) becomes a set of uncoupled modal equations:

$$\ddot{\tilde{u}}_{i,j} + \omega_{i,j}^2\tilde{u}_{i,j} = 0. \quad j = 1, \dots, n \tag{13}$$

Here, $\omega_{i,j}$ is the j^{th} natural frequency and $\tilde{u}_{i,j}$ is the corresponding modal displacement. Here, n denotes the number of DOFs in the CMS model. These modal equations admit the analytical solution

$$\tilde{u}_{i,j}(t) = \left(\frac{\tilde{u}_{0i,j}}{\sin\psi_{i,j}}\right)\sin\left(\omega_{i,j}t + \psi_{i,j}\right), \tag{14}$$

where $\tilde{u}_{0i,j}$ denotes the initial modal displacement at the instant when the system enters the i^{th} linear regime, and $\psi_{i,j}$ is the corresponding phase angle, defined as $\psi_{i,j} = \tan^{-1}(\omega_{i,j}\tilde{u}_{0i,j}/\dot{\tilde{u}}_{0i,j})$, with $\dot{\tilde{u}}_{0i,j}$ representing the initial modal velocity. The initial modal displacement and velocity are obtained by projecting the physical coordinates onto the modal space :

$$\begin{aligned}\tilde{u}_{0i,j} &= \boldsymbol{\Psi}_{i,j}^{T}\mathbf{M}_{ROM}(\mathbf{q}_0 - \boldsymbol{\beta}_i)\\ \dot{\tilde{u}}_{0i,j} &= \boldsymbol{\Psi}_{i,j}^{T}\mathbf{M}_{ROM}\dot{\mathbf{q}}_0.\end{aligned} \tag{15}$$

Here, $\mathbf{q}_0$ and $\dot{\mathbf{q}}_0$ denote the initial physical displacement and velocity in the reduced coordinates at the instant when the system enters the i^{th} linear regime, and $\boldsymbol{\Psi}_{i,j}$ represents the j^{th} mode shape of that regime. Once the modal response is determined, the response of the CMS model in the i^{th} linear regime can be reconstructed as

$$\mathbf{q} = \boldsymbol{\Psi}_i\tilde{\mathbf{u}}_i + \boldsymbol{\beta}_i. \tag{16}$$

Next, the incremental search process developed in [20] is modified to capture the nonlinear response of the wing-control surface structure by stitching together the piecewise-linear responses defined in Eq. (16). The free-play nonlinearity considered in this study is modeled using a trilinear stiffness characteristic, whereas the original incremental search process was developed only for systems with bilinear elements [19, 20, 25]. In this study, the transition between two linear regimes is determined based on the relationship between the nonlinear DOF θ_{nl} and the free-play angle δ, as defined in Eq.

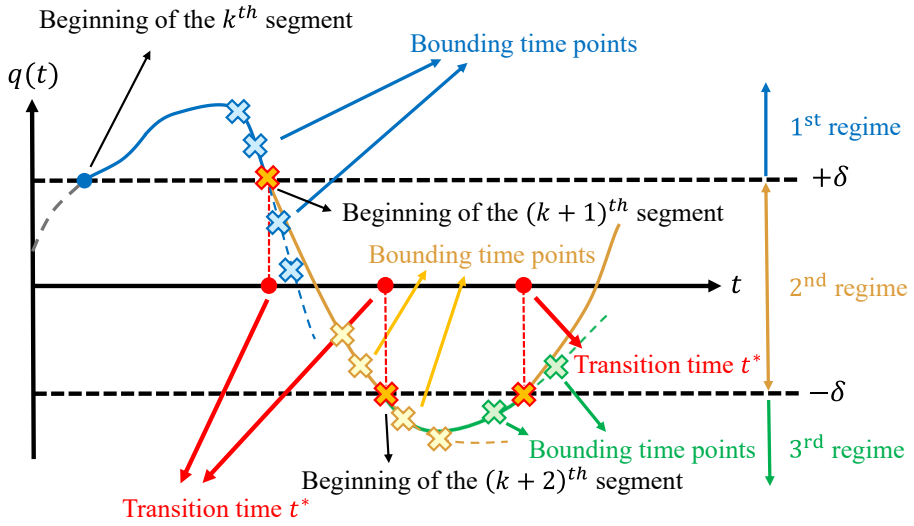


Fig. 2. Incremental search procedure and construction of the nonlinear response by stitching together analytical solutions across successive regime segments.

(1). The transition time t^*, at which the system switches between linear regimes, satisfies the following displacement compatibility condition:

$$\begin{aligned} &\boldsymbol{\Psi}_{i,1}\tilde{\mathbf{u}}_i(t^*) + \beta_{i,1} - \delta = 0, \quad \text{for transitions between the } 1^{\text{st}} \text{ and } 2^{\text{nd}} \text{ regime} \\ &\boldsymbol{\Psi}_{i,1}\tilde{\mathbf{u}}_i(t^*) + \beta_{i,1} + \delta = 0. \quad \text{for transitions between the } 2^{\text{nd}} \text{ and } 3^{\text{rd}} \text{ regime} \end{aligned} \tag{17}$$

Here, $\boldsymbol{\Psi}_{i,1}$ is the first row in the modal matrix $\boldsymbol{\Psi}_i$ and $\beta_{i,1}$ is the offset associated with the the nonlinear DOF in i-th linear regime. The transition time t^* represents the instant at which the system enters a new linear regime. Since Eq. (17) cannot be solved explicitly for t^*, the transition time is determined numerically. Specifically, the left-hand side of Eq. (17) is evaluated using the analytical modal solution in Eq. (14) with a prescribed time increment Δt. The first pair of consecutive time instants that bracket a sign change in the transition function $(\boldsymbol{\Psi}_{i,1}\tilde{\mathbf{u}}_i(t^*) + \beta_{i,1} \pm \delta)$ is identified. These two time instants are then used as the initial bracketing interval for MATLAB's root-finding function *fzero*, which determines the transition time t^*. Once the transition time for the k^{th} regime segment has been determined, the initial displacement and velocity of the $(k+1)^{th}$ segment are obtained by evaluating the displacement and velocity solutions (Eq. (14) and its derivative) at $t = t^*$. The analytical response $\mathbf{q}$ in the new linear regime is then computed using Eq. (16). By repeatedly performing this procedure for $k = 1,2,3,\cdots$, the complete nonlinear response of the wing–control surface structure is obtained by stitching together the analytical solutions across successive regime segments, as illustrated in Fig. 2. The two consecutive time instants used to bracket each transition are labeled as "bounding time points"

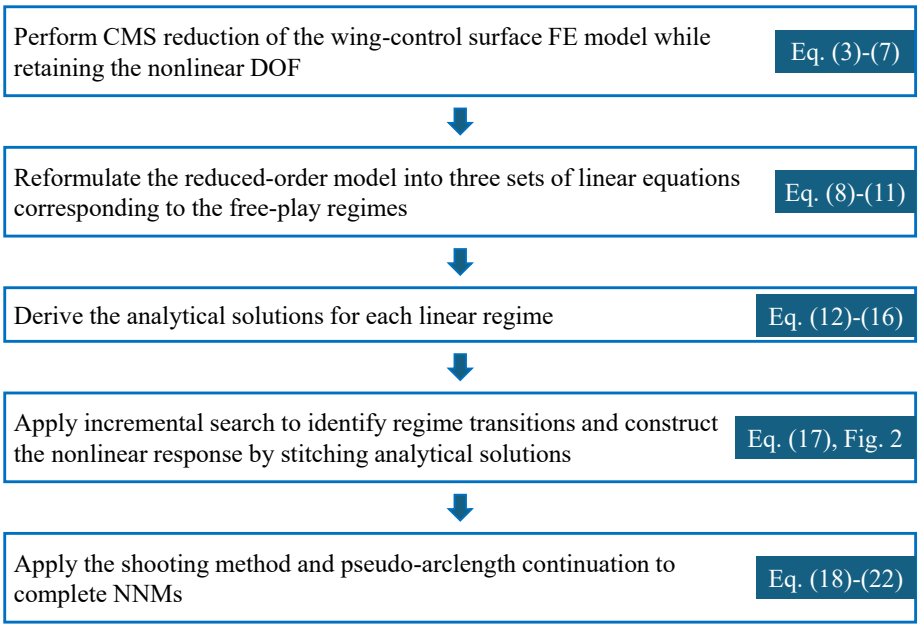


Fig. 3. The overall computational procedure of the proposed CMS-HCF.

Finally, the pseudo-arclength continuation scheme proposed in [18] is integrated with the piecewise-analytical response computation described above (Fig. 2) to compute NNMs of the system. During the continuation process, the state vector is defined as $\mathbf{z} = [\mathbf{q}^T;\ \dot{\mathbf{q}}^T]^T$. The continuation procedure begins by determining the initial state $\mathbf{z}_0 = [\mathbf{q}_0^T;\ \dot{\mathbf{q}}_0^T]^T$ and the corresponding fundamental period T that satisfy the periodicity condition $\mathbf{z}(t, \mathbf{z}_0) = \mathbf{z}(t + T, \mathbf{z}_0)$. The periodic solution $(\mathbf{z}_0, T)$ is obtained using the shooting method [26], in which the shooting function is defined as

$$\mathbf{G}(\mathbf{z}_0, T) = \mathbf{z}(t + T, \mathbf{z}_0) - \mathbf{z}(t, \mathbf{z}_0) = \mathbf{0} \tag{18}$$

The Newton-Raphson method is employed to iteratively update $(\mathbf{z}_0, T)$ until the residual of Eq. (18) satisfies a prescribed convergence tolerance. Once a periodic solution has been obtained, the pseudo-arclength continuation method is employed to trace the frequency–energy dependence of the NNMs. The continuation procedure consists of a predictor step followed by a corrector step. In the predictor step, a trial solution $(\tilde{\mathbf{z}}_0, \tilde{T})$ is generated from the previously converged solution $(\mathbf{z}_0, T)$ according to

$$\begin{bmatrix} \tilde{\mathbf{z}}_0 \\ \tilde{T} \end{bmatrix} = \begin{bmatrix} \mathbf{z}_0 \\ T \end{bmatrix} + s \begin{bmatrix} \mathbf{p}_z \\ p_T \end{bmatrix}, \tag{19}$$

where s denotes the predictor step size, and $\mathbf{p} = [\mathbf{p}_z^T;\ p_T]^T$ is the tangent vector to the continuation branch. The tangent vector satisfies the orthogonality condition:

$$\begin{bmatrix} \frac{\partial \mathbf{G}}{\partial \mathbf{z}_0} & \frac{\partial \mathbf{G}}{\partial T} \end{bmatrix} \begin{bmatrix} \mathbf{p}_z \\ p_T \end{bmatrix} = \begin{bmatrix} \mathbf{0} \\ 0 \end{bmatrix}, \tag{20}$$

and is obtained from the null space of the Jacobian matrix in Eq. (20). The predicted solution is subsequently refined during the corrector step according to

$$\begin{aligned} \mathbf{z}_0^{(l+1)} &= \mathbf{z}_0^{(l)} + \Delta \mathbf{z}_0^{(l)}, \\ T^{(l+1)} &= T^{(l)} + \Delta T^{(l)}, \end{aligned} \tag{21}$$

where l denotes the iteration index. The correction terms $(\Delta \mathbf{z}_0^{(l)}, \Delta T^{(l)})$ are obtained by solving

$$\begin{bmatrix} \frac{\partial \mathbf{G}}{\partial \mathbf{z}_0} & \frac{\partial \mathbf{G}}{\partial T} \\ \mathbf{p}_z^T & p_T \end{bmatrix} \begin{bmatrix} \Delta \mathbf{z}_0^{(l)} \\ \Delta T^{(l)} \end{bmatrix} = \begin{bmatrix} -\mathbf{G}^{(l)}\left(\mathbf{z}_0^{(l)}, T^{(l)}\right) \\ 0 \end{bmatrix}. \tag{22}$$

Here, the Jacobian matrices are evaluated numerically. The corrector iterations continue until the periodicity and continuation constraints satisfy the prescribed convergence tolerances.

By repeatedly applying the predictor and corrector steps, a sequence of periodic solutions $(\mathbf{z}_0, T)$ satisfying Eq. (18) is obtained. These solutions define the frequency–energy dependence of an NNM branch, where the oscillation frequency is calculated from the corresponding period T, and the energy is evaluated from the total energy associated with the initial conditions $\mathbf{z}_0$. A flowchart of the proposed CMS–HCF framework is presented in Fig. 3.

3 Results

The NNMs of a wing–control surface structure are analyzed using the proposed CMS–HCF framework, and the results are compared with those obtained using the conventional NCF.

3.1 Construction of the Reduced-Order Model

A FE model of an aircraft wing with a control surface, based on a configuration similar to that reported in [1], was developed in ANSYS, and its geometry is illustrated in Fig. 4. The model was discretized using SHELL181 elements [27] with a thickness of 20 mm. The wing structure was assumed to be made of titanium, characterized by a Young's modulus of $E = 120$ GPa, a density of $\rho = 4{,}540\ \mathrm{kg/m^3}$, and a Poisson's ratio of $\upsilon = 0.36$. The lower boundary of the wing was fixed, while the control surface was allowed to rotate about the hinge axis. A mesh convergence study was carried out based on the linear natural frequencies, and the converged FE model contained 379

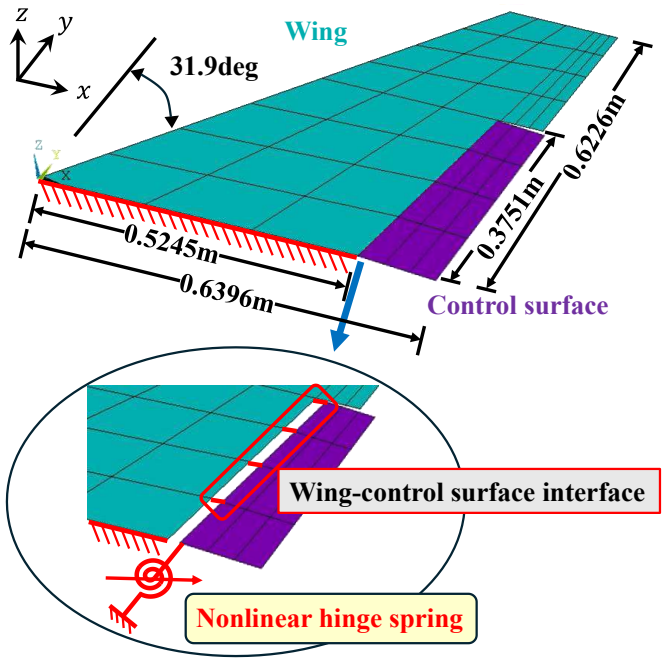


Fig. 4. The finite element model of aircraft wing with a control surface.

DOFs. The corresponding mass and stiffness matrices were extracted from ANSYS and exported to MATLAB for subsequent reduced-order modeling and NNM analysis.

The Craig–Bampton CMS method was then employed to reduce the FE model. The resulting constraint mode and the eight lowest fixed-interface normal modes are illustrated in Fig. 5. The constraint mode corresponds to the static deformation induced by applying a unit rotational displacement at the nonlinear DOF of the control surface hinge. The fixed-interface normal modes represent the linear mode shapes of the structure with the nonlinear DOF held fixed. These modes collectively form the modal basis for constructing the reduced-order models.

To assess the accuracy and convergence of the reduced-order models, the linear natural frequencies of the 2-DOF, 3-DOF, 5-DOF, 7-DOF, and 9-DOF models are compared with those of the full FE model, as summarized in Table 1. These reduced-order models were constructed using the constraint mode together with the lowest one, two, four, six, and eight fixed-interface normal modes, respectively. As shown in Table 1, the predicted linear natural frequencies progressively converge toward those of the full FE model as the number of retained fixed-interface modes increases. For the models considered in this study, the N-DOF reduced-order model accurately predicts the first N-1 linear natural frequencies, with relative errors below 1.22%. However, convergence of the linear natural frequencies does not necessarily guarantee an accurate

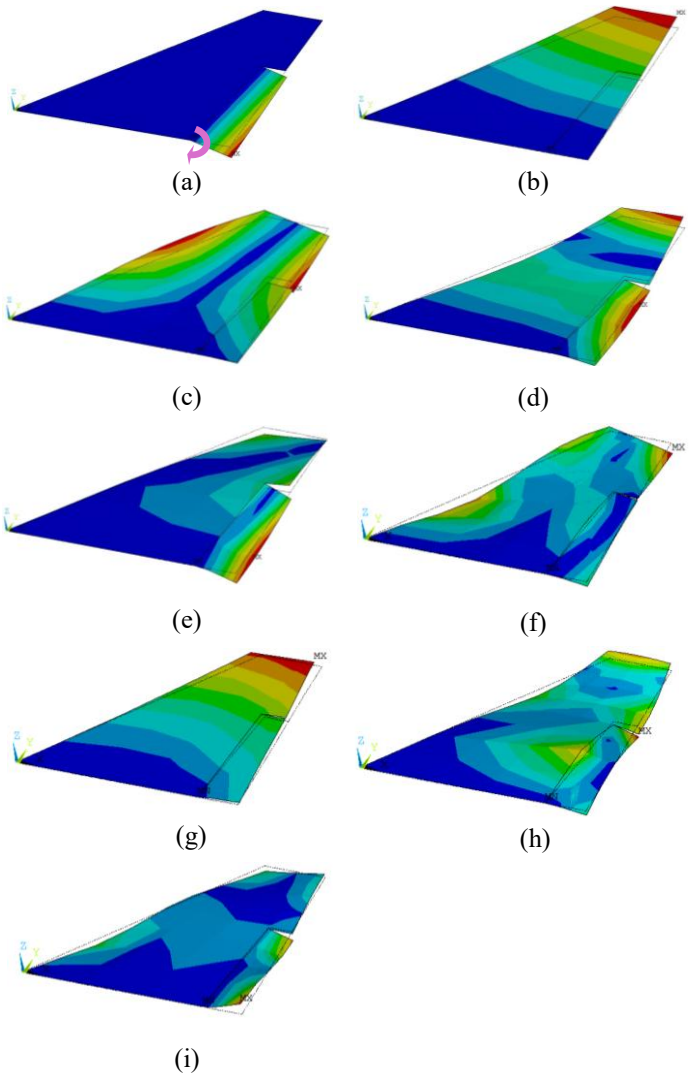


Fig. 5. The mode shapes used to construct reduced-order models: (a) constraint mode; (b)-(i) the eight lowest fixed-interface normal modes.

representation of the nonlinear modal characteristics. Therefore, the convergence of the predicted NNMs with respect to the number of retained fixed-interface modes is further investigated in the subsequent section

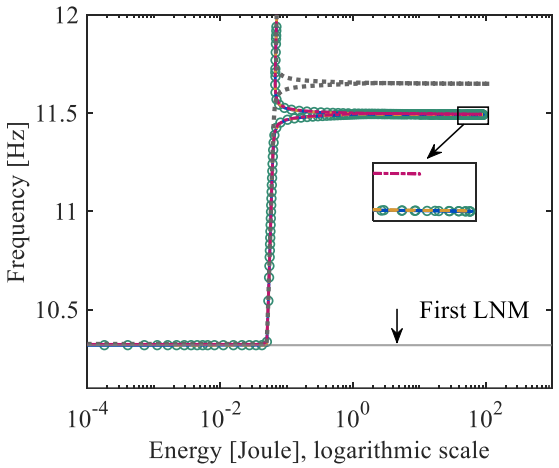
Table 1. Linear natural frequencies of full and reduced order models

Linear natural frequencies	Full FE model	2-DOF model (relative error)	3-DOF model (relative error)	5-DOF model (relative error)	7-DOF model (relative error)	9-DOF model (relative error)
1st mode	10.319 Hz	10.325 Hz (0.06%)	10.323 Hz (0.04%)	10.319 Hz (0.00%)	10.319 Hz (0.00%)	10.319 Hz (0.00%)
2nd mode	57.458 Hz	58.246 Hz (1.37%)	57.471 Hz (0.02%)	57.458 Hz (0.00%)	57.458 Hz (0.00%)	57.458 Hz (0.00%)
3rd mode	221.920 Hz		229.061 Hz (3.21%)	221.945 Hz (0.01%)	221.927 Hz (0.00%)	221.922 Hz (0.00%)
4th mode	308.247 Hz			308.428 Hz (0.05%)	308.323 Hz (0.02%)	308.267 Hz (0.01%)
5th mode	619.926 Hz			1344.672 Hz (116.91%)*	620.526 Hz (0.10%)	620.066 Hz (0.02%)
6th mode	863.380 Hz				876.530 Hz (1.52%)	864.808 Hz (0.17%)
7th mode	876.530 Hz					876.530 Hz (0.00%)
8th mode	962.434 Hz					974.215 Hz (1.22%)
9th mode	1209.561 Hz					2708.119 Hz (123.89%)

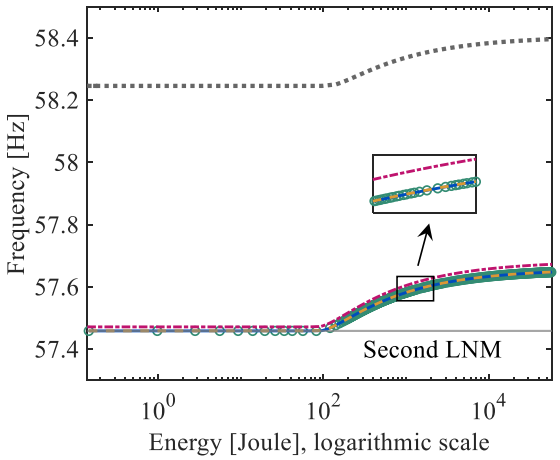
3.2 Model-Reduction Convergence and Validation of NNM Analysis

In this study, the piecewise-linear restoring torque at the control surface hinge is described by Eq. (1), with stiffness parameters set to $k = 40\ \mathrm{Nm/rad}$ and $k^* = 400\ \mathrm{Nm/rad}$, consistent with those employed in [1]. A nonzero central stiffness k is retained within the free-play region, providing a more general representation of the hinge behavior with finite residual stiffness. The free-play angle is specified as $\delta = 0.05\ \mathrm{rad}$.

Following the convergence study based on the linear natural frequencies, the convergence of the NNM solutions was further examined using the 2-, 3-, 5-, 7-, and 9-DOF reduced-order models. The frequency–energy curves of the first and second NNM families are presented in Figs. 6(a) and 6(b), respectively. The corresponding linear normal mode (LNM) frequencies are also included for reference. For the first NNM family shown in Fig. 6(a), noticeable discrepancies are observed for the 2- and 3-DOF models after the branch enters the internal resonance region, whereas the solutions progressively converge as additional fixed-interface modes are retained. The curves obtained using the 5-, 7-, and 9-DOF models are nearly indistinguishable over the plotted energy range, including the internal resonance region. A similar convergence trend is



(a)



(b)

Fig. 6. Convergence of the (a) first and (b) second NNM families predicted by the 2-, 3-, 5-, 7-, and 9-DOF reduced-order models. The corresponding frequency–energy curves are shown in (gray ·), (red · –), (orange – –), (darkblue –), and (green ◦), respectively.

observed for the second NNM family in Fig. 6(b). The 2- and 3-DOF models overpredict the NNM frequency, whereas the predictions from the 5-, 7-, and 9-DOF models exhibit close agreement. These results indicate that the 5-DOF reduced-order model provides sufficiently converged predictions of the first two NNM families. Therefore, the 5-DOF model is adopted for the subsequent validation and nonlinear modal

analyses, providing an appropriate balance between computational efficiency and solution accuracy.

To validate the NNM solutions obtained using the proposed CMS–HCF, a two-stage validation procedure was performed, with the corresponding results presented in Fig. 7. In the first stage, the first NNM branch of the 5-DOF reduced-order model was independently computed using CMS–HCF and CMS–NCF. As shown in Fig. 7(a), the frequency–energy curves obtained using the two methods overlap over the entire energy range, including the tongue-shaped region of the NNM branch, demonstrating the numerical consistency between the two continuation frameworks. Direct computation of the complete frequency–energy curve using the full-order FE model is computationally prohibitive on the workstation employed in this study. Therefore, in the second stage of validation, three representative periodic solutions, indicated by the triangular (▲), square (■), and circular (●) markers in Fig. 7(a), were selected for comparison with transient simulations of the full-order FE model. For each selected solution, the initial condition obtained from CMS–HCF in the reduced coordinates was reconstructed in the full physical coordinates using the Craig–Bampton transformation matrix defined in Eq. (6):

$$\mathbf{x}_0 = \boldsymbol{\alpha}\mathbf{q}_0. \tag{23}$$

The reconstructed displacement vector $\mathbf{x}_0$ was then prescribed as the initial displacement of the full FE model in ANSYS APDL, with the initial velocity set to zero. The subsequent free-vibration response of the full FE model was computed using transient structural analysis with the implicit Newmark method. This procedure enables an assessment of the extent to which the dynamic characteristics predicted by the 5-DOF CMS–HCF model are reproduced in the full-order FE response.

Fig. 7(b)–(d) compare the corresponding time histories and FFT spectra of the three representative periodic solutions, corresponding to the triangular (▲), square (■), and circular (●) markers in Fig. 7(a), respectively. For each solution, the leftmost panel compares the time-domain responses obtained using CMS–HCF, CMS–NCF, and the full-order FE model, while the three panels to the right show their respective FFT spectra. For the low-energy solution in Fig. 7(b), the three methods produce nearly identical time histories, with the response dominated by a single frequency component at 10.80 Hz. For the solution within the tongue region shown in Fig. 7(c), CMS–HCF and CMS–NCF again produce nearly identical time histories and frequency spectra. In addition to the fundamental component at approximately 11.49 Hz, both reduced-order solutions contain a pronounced component at 57.47 Hz, which is approximately five times the fundamental frequency. This component therefore corresponds to the fifth harmonic of the fundamental oscillation and is associated with the second NNM family, suggesting a 1:5 internal resonance between the first and second modes. The full FE model, initialized using the reconstructed CMS–HCF solution, also exhibits frequency components near 11.49 and 57.47 Hz, providing further evidence consistent with this modal interaction. Additional higher-frequency components, including those near 218.40 and 310.35 Hz, are observed in the full-order FE response but are not captured by the 5-DOF reduced-order model. These additional components may arise because the initial

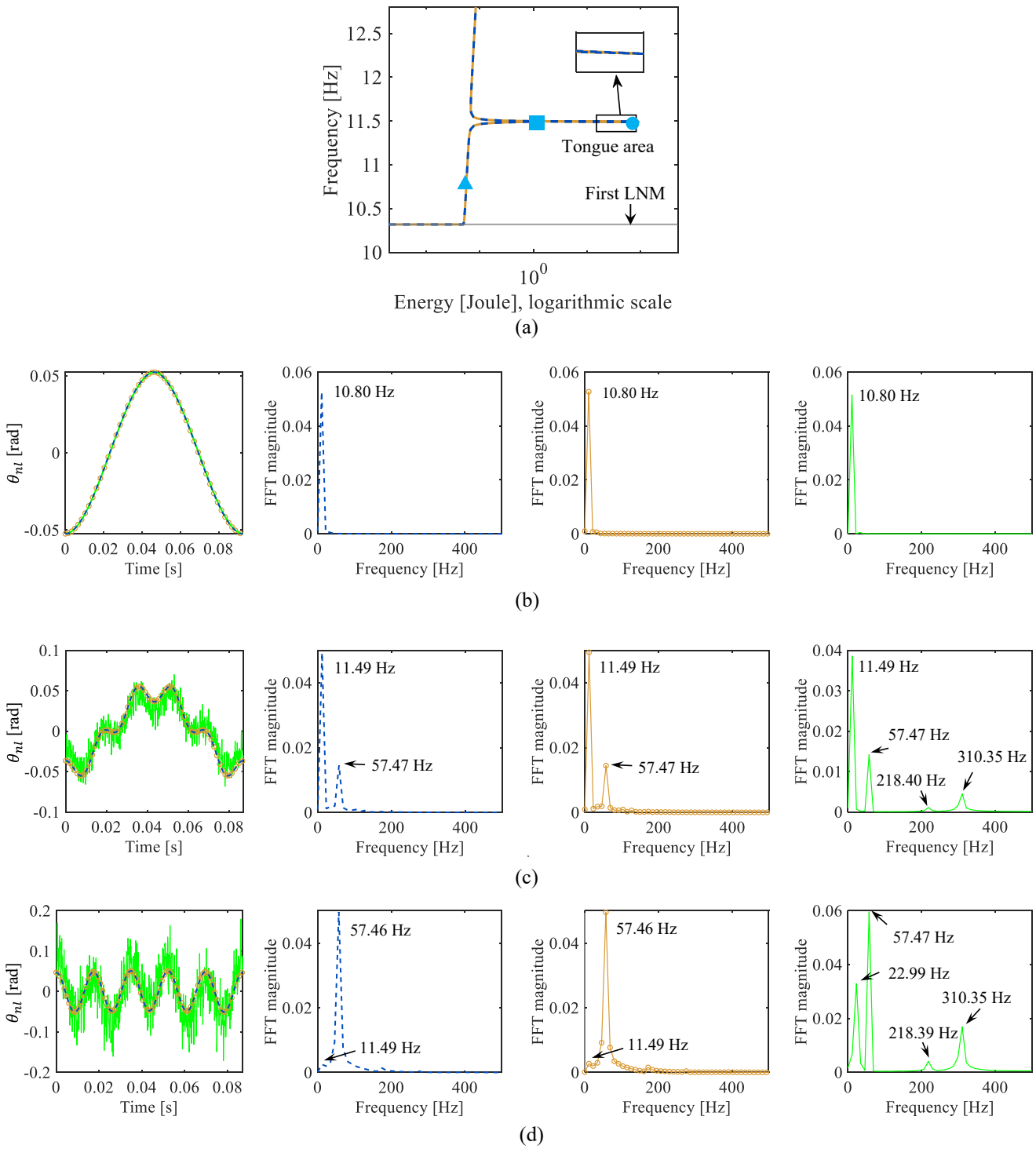


Fig. 7. (a) Frequency–energy curve of the first NNM branch of the 5-DOF model computed using the proposed CMS–HCF and CMS–NCF frameworks. Panels (b), (c), and (d) present the time- and frequency-domain responses corresponding to the triangular, square, and circular markers in panel (a), respectively. For each selected solution, the leftmost panel compares the time-domain responses obtained using CMS–HCF, CMS–NCF, and the full-order FE model simulated using the implicit Newmark method, represented by the (blue – –), (orange o), and (green –), respectively. The three panels to the right present the corresponding FFT spectra in the same order.

displacement reconstructed from the reduced-order solution using Eq. (23) does not necessarily correspond to an exact periodic solution of the full-order FE system. Consequently, the reconstructed initial condition may excite higher-frequency structural modes that are not retained in the reduced-order model.

As the solution progresses toward the tip of the tongue-shaped region, as shown in Fig. 7(d), the component near 57.46 Hz becomes dominant. The CMS–HCF and CMS–NCF solutions remain in close agreement and contain both the fundamental component near 11.49 Hz and the dominant fifth-harmonic component near 57.46 Hz. The full FE response is likewise dominated by the component near 57.47 Hz, although multiple higher-frequency components are also observed. The consistent emergence and subsequent dominance of the fifth-harmonic component in both the reduced- and full-order models are consistent with the interpretation that the tongue-shaped feature of the first NNM branch is associated with a 1:5 internal resonance with the second NNM family.

The second NNM family was validated in a similar manner. Fig. 8(a) compares the frequency–energy curves obtained using CMS–HCF and CMS–NCF for the 5-DOF model. The two curves are nearly indistinguishable over the plotted energy range. A representative periodic solution, indicated by the square marker (□) in the enlarged region of Fig. 8(a), was selected for further comparison with the full FE model. As shown in Fig. 8(b), CMS–HCF and CMS–NCF predict nearly identical time histories and FFT spectra, with the response dominated by a frequency component at approximately 57.60 Hz. The full FE model also exhibits a dominant component at the same frequency, although additional higher-frequency components are present in its response. The agreement in the dominant oscillation frequency supports the ability of the 5-DOF reduced-order model to capture the principal dynamics associated with the second NNM family.

Overall, the results in Figs. 7 and 8 demonstrate that the proposed CMS–HCF accurately reproduces the first two NNM branches obtained using CMS–NCF, including the tongue-shaped feature associated with the 1:5 internal resonance. Comparisons with the full FE model further demonstrate that the 5-DOF reduced-order model captures the dominant frequencies and modal interactions associated with the first two NNM families. Although additional higher-frequency components are observed in the full FE simulations, the dominant low-frequency components remain consistent with the reduced-order predictions. In particular, the 5-DOF model successfully retains the fifth-harmonic component associated with the 1:5 internal resonance between the first and second NNM families, demonstrating that the reduced-order model preserves the principal nonlinear modal interactions despite the substantial reduction from 379 to 5 DOFs. These results therefore support the accuracy of CMS–HCF for NNM computation and demonstrate the capability of the CMS reduced-order model to capture the principal nonlinear modal characteristics associated with the first two NNM families of the full wing–control surface structure.

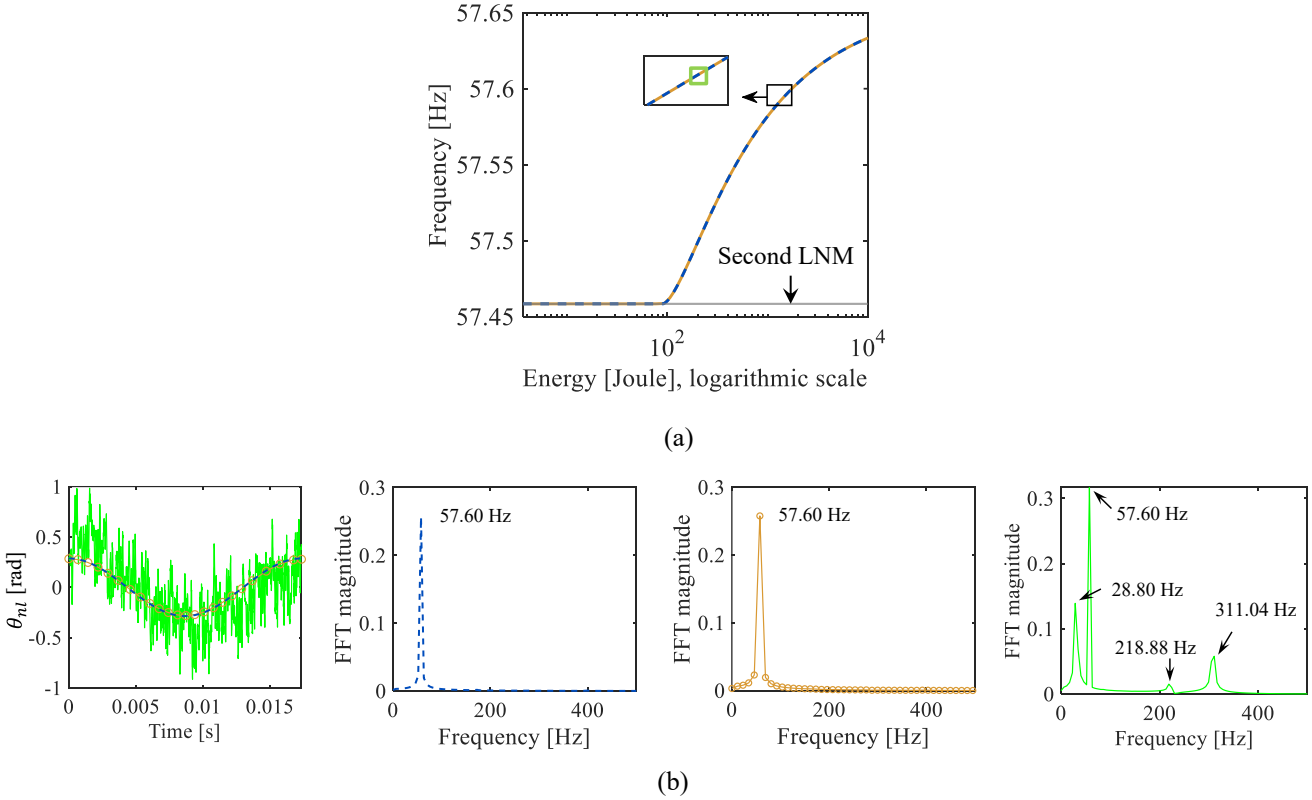
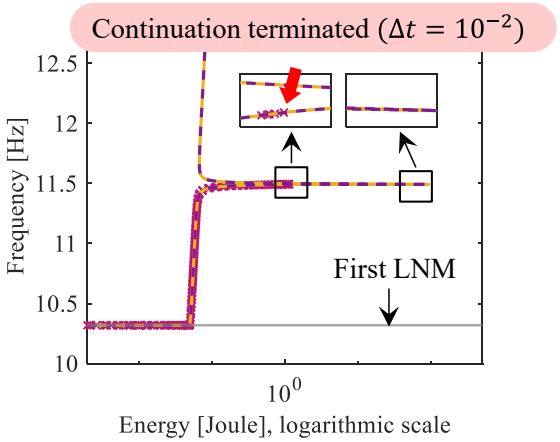
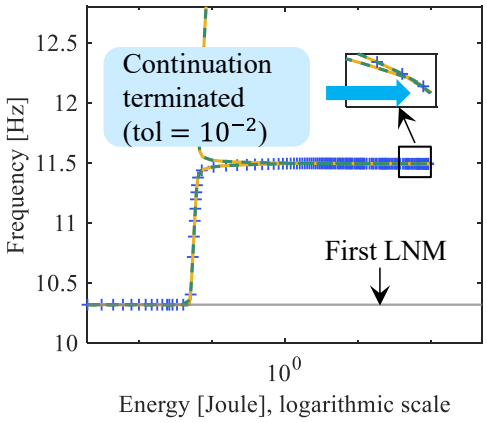


Fig. 8. (a) Frequency–energy curve of the second NNM branch of the 5-DOF reduced-order model computed using CMS–HCF and CMS–NCF. The inset shows an enlarged view of the boxed region, and the square marker indicates the solution selected for further analysis. (b) Time- and frequency-domain responses of the selected solution. The leftmost panel compares the time-domain responses obtained using CMS–HCF, CMS–NCF, and the full-order FE model simulated using the implicit Newmark method, represented by (blue – –), (orange o), and (green –), respectively. The three panels to the right present the corresponding FFT spectra in the same order.



(a)



(b)

Fig. 9. The frequency-energy plots of the first NNM curve of the 5-DOF model computed using (a) CMS-HCF and (b) CMS-NCF with different control parameters. For CMS–HCF, time increments of $10^{-2}, 10^{-3}$, and 10^{-4}s are represented by (red ×), (yellow −), and (purple − −), respectively. For CMS–NCF, relative and absolute tolerances of $10^{-9}, 10^{-10}$, and 10^{-11}, represented by (blue +), (yellow −), and (green − −), respectively. The enlarged views highlight the regions where continuation terminates prematurely under the least restrictive numerical settings.

3.3 Computational Efficiency of CMS-HCF and CMS-NCF

To evaluate the computational efficiency of the proposed CMS–HCF, the first NNM branch of the 5-DOF model was computed using CMS–HCF and CMS–NCF while systematically varying the numerical control parameters associated with each method. For CMS–HCF, the time increment Δt used in the incremental search process of the HSNC method was varied among $\Delta t = 10^{-2}$, 10^{-3}, and 10^{-4} s, and the corresponding frequency–energy curves are presented in Fig. 9(a). The largest time increment, $\Delta t = 10^{-2}$, failed to trace the NNM branch through the internal resonance region, whereas $\Delta t = 10^{-3}$ and $\Delta t = 10^{-4}$ s produced nearly identical frequency–energy curves. Therefore, $\Delta t = 10^{-3}$ was selected for the subsequent CPU-time comparison because it represents the largest time increment among those tested that provides a converged NNM solution without unnecessary computational cost.

For CMS–NCF, numerical time integration was performed using the MATLAB ODE45 solver. The relative and absolute tolerances were simultaneously varied among 10^{-9}, 10^{-10}, and 10^{-11}, and the corresponding frequency-energy curves are presented in Fig. 9(b). The least restrictive tolerance, 10^{-9}, failed to trace the complete NNM branch near the tip of the tongue-shaped region, whereas 10^{-10} and 10^{-11} successfully traced the branch and produced nearly indistinguishable frequency–energy curves. Accordingly, relative and absolute tolerances of 10^{-10} were adopted for the subsequent CPU-time comparison. These parameter-selection studies ensure that the computational costs of CMS–HCF and CMS–NCF are compared using the least restrictive numerical settings among those tested that provide converged NNM solutions for each framework.

Using these settings, both methods successfully traced the complete first NNM branch and produced essentially identical frequency–energy curves. For the 5-DOF model, CMS–HCF required 127.5 s to compute 290 continuation points, corresponding to an average CPU time of 0.44 s per point. In comparison, CMS–NCF required 2107.3 s for 301 continuation points, corresponding to 7.00 s per point. Thus, CMS–HCF provides an approximately 15.9-fold speedup in CPU time per continuation point while maintaining comparable NNM predictions.

To further investigate the computational scalability of the proposed framework, the same comparison was performed using the 5-, 7-, 9-, and 10-DOF reduced-order models, with the results summarized in Table 2 and Fig. 10. For each model dimension, the numerical control parameters for CMS–HCF and CMS–NCF were selected following the same convergence criterion described above to provide comparable solution accuracy. As the model dimension increases, the computational cost of CMS–NCF increases substantially, from 7.0 s per continuation point for the 5-DOF model to 25.8 s per point for the 10-DOF model. In contrast, the computational cost of CMS–HCF remains within approximately 0.4–0.7 s per point over the same range of model dimensions. Consequently, the computational advantage of CMS–HCF becomes increasingly pronounced as the model dimension increases. Based on the values in Table 2, the speedup in CPU time per continuation point increases from approximately 15.9× for the 5-DOF model to approximately 35.6× for the 10-DOF model. These results demonstrate that, in addition to providing accurate NNM predictions, the proposed CMS–HCF offers

substantially improved computational efficiency over the investigated range of model dimensions compared with the conventional CMS–NCF.

Table 2. Comparison of CPU times and computational speedups for computing the first NNM branch using CMS–NCF and CMS–HCF with 5-, 7-, 9-, and 10-DOF reduced-order models.

Model	CMS-NCF	CMS-HCF	Speedup
5-DOF	7.00 s / point (2107.3 s, 301 points)	0.44 s / point (127.5 s, 290 points)	15.9×
7-DOF	10.86 s / point (3270.2 s, 301 points)	0.65 s / point (145.8 s, 226 points)	16.8×
9-DOF	17.79 s / point (4179.5 s, 235 points)	0.50 s / point (136.2 s, 271 points)	35.4×
10-DOF	25.79 s / point (7968.2 s, 309 points)	0.73 s / point (179.8 s, 248 points)	35.6×

Note: Average CPU time per continuation point is shown first, followed by total CPU time and number of continuation points. Speedups are calculated using unrounded values.

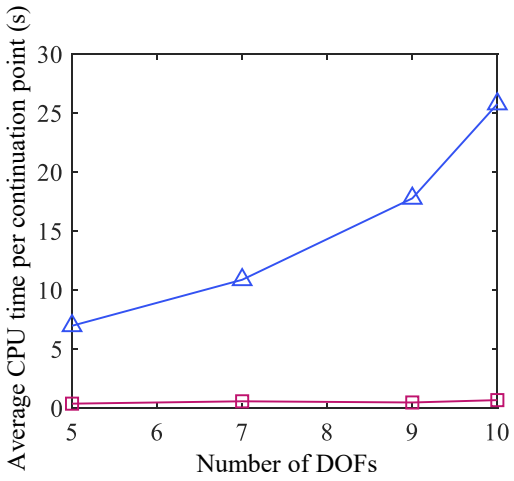


Fig. 10. Comparison of the average CPU time per continuation point for CMS–HCF and CMS–NCF for the 5-, 7-, 9-, and 10-DOF reduced-order models. The red curve with square markers (□) represents CMS–HCF, while the blue curve with triangular markers (△) represents CMS–NCF.

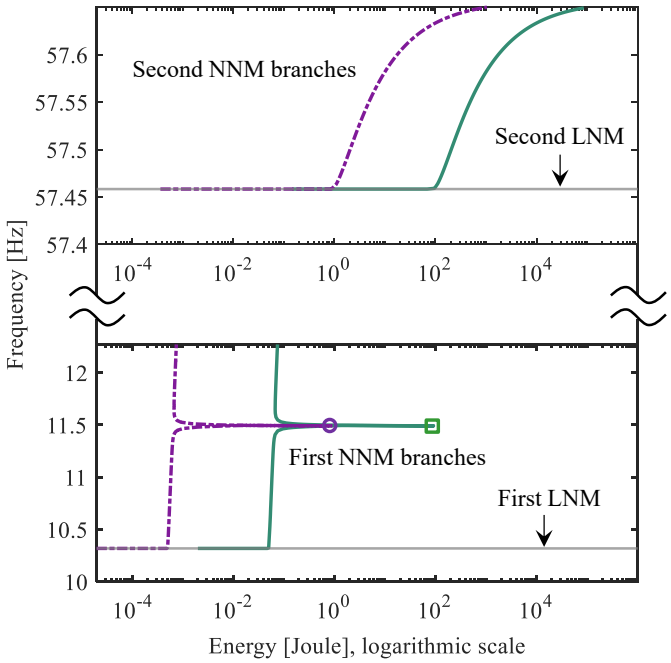


Fig. 11. The frequency-energy plots of the first and the second NNM families of the 5-DOF reduced-order model for free-play angles of $\delta = 0.05$ and $\delta = 0.005$ rad, represented by (green —) and (purple · —), respectively. The corresponding linear natural frequencies are also indicated for reference.

3.4 Effects of Free-Play Angle and Central Stiffness on NNMs

Next, the free-play angle was reduced from $\delta = 0.05$ rad to $\delta = 0.005$ rad to investigate its effect on the NNMs. The corresponding NNM results are shown in Fig. 11. Reducing the free-play angle shifts both the first and second NNM branches toward lower energy levels, indicating that the piecewise-linear nonlinearity is activated at a smaller oscillation amplitude. Because the free-play angle is reduced by one order of magnitude, the energy level associated with the onset of nonlinear behavior decreases by approximately two orders of magnitude. This scaling is consistent with the quadratic dependence of the mechanical energy on the free-play angle for fixed stiffness parameters. Despite this shift in energy, the overall frequency ranges and shapes of the NNM branches remain nearly unchanged. In particular, the tongue-shaped region retains a similar structure because the same 1:5 internal resonance between the first and second NNM families persists. Thus, reducing the free-play angle primarily lowers the energy level at which the nonlinear modal interaction occurs without substantially altering the underlying modal characteristics.

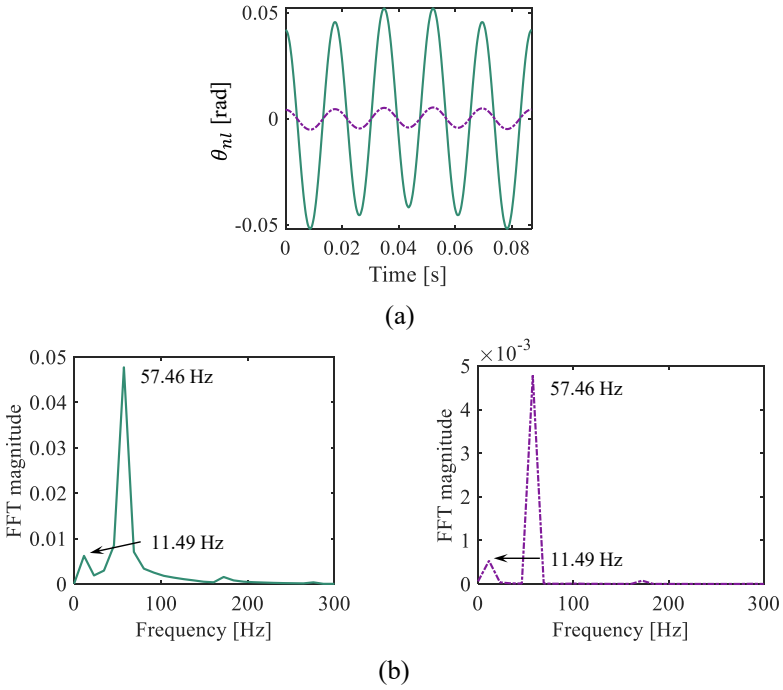


Fig. 12. Comparison of (a) time-domain responses and (b) corresponding FFT spectra of the nonlinear rotational DOF for two free-play angles, $\delta = 0.05$ and $\delta = 0.005$ rad, at representative solutions within the tongue-shaped regions of the first NNM family. The results for $\delta = 0.05$ rad and $\delta = 0.005$ rad are represented by (green $-$) and (purple $\cdot -$), respectively.

Fig. 12 compares the time-domain responses of the nonlinear DOF at representative high-energy points within the tongue-shaped regions, indicated by the green square (□) and purple circle (○) markers in Fig. 11, for free-play angles of $\delta = 0.05$ and $\delta = 0.005$ rad, respectively. The responses exhibit similar waveform characteristics, with the oscillation amplitudes differing by approximately one order of magnitude. Their FFT spectra also reveal nearly identical dominant frequency components at approximately 11.49 and 57.46 Hz, indicating that the 1:5 internal-resonance characteristics are preserved despite the reduction in the free-play angle. These results further indicate that the modal interaction within the tongue-shaped region remains essentially unchanged as the free-play angle is reduced, while the energy level at which this interaction occurs decreases substantially. Overall, the results in Figs. 11 and 12 demonstrate that the free-play angle primarily controls the energy scale at which nonlinear behavior emerges. A smaller free-play angle causes the system to encounter the outer stiffness regimes at a lower oscillation amplitude and therefore activates the nonlinear modal behavior and associated internal resonance at a lower energy level. However, the frequency characteristics and modal-interaction mechanism remain unchanged.

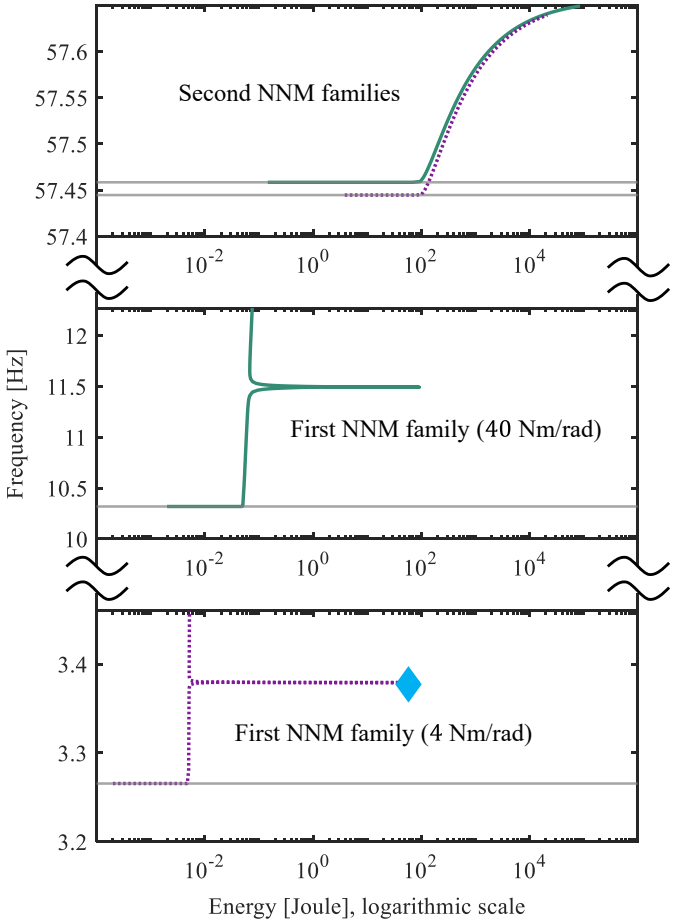


Fig. 13. Comparison of the first and second NNM families of the 5-DOF reduced-order model for two central-stiffness values, $k = 4$ and $40\ \mathrm{Nm/rad}$, with $k^* = 400\ \mathrm{Nm/rad}$ and $\delta = 0.05$ rad. The results for $k = 4$ and $40\ \mathrm{Nm/rad}$ are represented by the (purple ·) and (green —), respectively. The blue diamond marker indicates the periodic solution selected for the time- and frequency-domain analyses in Fig. 14.

To further investigate the NNM characteristics under a more pronounced free-play condition, the central stiffness was reduced to $k = 4\ \mathrm{Nm/rad}$, while $k^* = 400\ \mathrm{Nm/rad}$ and $\delta = 0.05$ rad were retained. The substantially smaller central stiffness provides a closer approximation to an ideal free-play system and increases the stiffness contrast between the inner and outer regimes, allowing its influence on the NNM branches and modal interactions to be examined. Fig. 13 compares the first and second NNM families obtained with $k = 4\ \mathrm{Nm/rad}$ with those obtained using the original

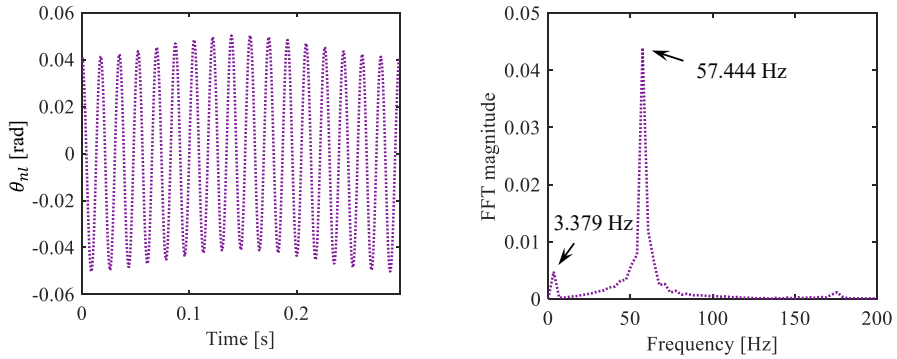


Fig. 14. (a) Time-domain response and (b) corresponding FFT spectrum of the nonlinear rotational DOF for the representative periodic solution indicated by the diamond marker in Fig. 13, corresponding to $k = 4\ \mathrm{Nm/rad}$.

value of $k = 40\ \mathrm{Nm/rad}$. Reducing the central stiffness substantially decreases the first linear natural frequency and shifts the first NNM family toward a much lower frequency range. In contrast, the second NNM family experiences only a relatively small frequency shift. Consequently, the frequency separation between the first and second NNM families increases substantially, altering the internal-resonance condition between the two modes. The first tongue-shaped regions obtained for the two stiffness values are also compared in Fig. 13.

A representative periodic solution within the first tongue-shaped region for $k = 4\ \mathrm{Nm/rad}$, indicated by the diamond marker (◆) in Fig. 13, was selected for further analysis. The corresponding time-domain response of the nonlinear rotational DOF and its FFT spectrum are presented in Figs. 14(a) and 14(b), respectively. The FFT spectrum reveals frequency components at approximately 3.379 and 57.444 Hz, corresponding to a frequency ratio of approximately 1:17. Together with the tongue-shaped feature of the NNM branch, these components suggest a 1:17 internal resonance between the first and second NNM families. In comparison with the 1:5 internal resonance observed for the original central stiffness, reducing k substantially lowers the frequency of the first NNM family while producing a much smaller change in the second. The resulting increase in the modal-frequency ratio leads to a higher-order internal resonance between the first and second NNM families. These results demonstrate that, unlike the free-play angle, which primarily controls the energy level at which nonlinear modal interactions are activated, the central stiffness can significantly alter the modal-frequency relationship and consequently the order of internal resonance.

4 Conclusions and Future Work

This study developed an efficient CMS–HCF framework for analyzing the nonlinear normal modes (NNMs) of an aircraft wing–control surface structure with free-play nonlinearity. To the best of the authors' knowledge, this is the first study to investigate nonlinear modal interactions in such a structure using a high-dimensional finite element (FE) model that captures both structural flexibility and localized free-play nonlinearity. The Craig–Bampton CMS method was employed to reduce the FE model while retaining the nonlinear DOF, and the HCF was integrated with the reduced-order model to enable efficient NNM computation. Comparisons with CMS–NCF and transient simulations of the full FE model demonstrated that the proposed framework accurately predicts the first two NNM families and captures the dominant nonlinear modal characteristics associated with internal resonance. Moreover, CMS–HCF achieved substantial computational savings over CMS–NCF, with speedups ranging from approximately 16 times for the 5-DOF model to 36 times for the 10-DOF model.

The parametric studies revealed distinct effects of the free-play angle and central stiffness on the nonlinear modal behavior. Reducing the free-play angle primarily shifted the NNM branches and associated internal-resonance regions toward lower energy levels without substantially altering their frequency characteristics. In contrast, reducing the central stiffness significantly changed the modal-frequency relationship and consequently altered the order of internal resonance between the first and second NNM families. These results demonstrate that the proposed CMS–HCF provides an accurate and computationally efficient approach for investigating nonlinear modal characteristics of structural systems with localized piecewise-linear nonlinearities.

Future work will focus on extending the proposed CMS–HCF framework to nonconservative dynamical systems, enabling the incorporation of aerodynamic forces and fluid–structure interactions into the reduced-order structural model. This extension will require further development of the current framework to account for nonconservative aerodynamic loading and its influence on the periodic responses and stability of the coupled system. By integrating the extended framework with high-fidelity computational fluid dynamics or reduced-order aerodynamic models, future studies will investigate nonlinear aeroelastic phenomena in flexible wing–control surface structures with free-play nonlinearities. Particular emphasis will be placed on the computation and stability analysis of periodic responses, providing a foundation for investigating aeroelastic instabilities, including flutter and limit-cycle oscillations.

Conflict of Interest

The authors declare that they have no competing interests that could have influenced the work reported in this manuscript.

Acknowledgement

This research was supported by the National Science and Technology Council (NSTC), Taiwan, under Grant Nos. NSTC 114-2628-E-007-013 and NSTC 115-2628-E-007-007. The first author, Chin-Yi Chang, received financial support from the NSTC Graduate Research Fellowship Program. A preliminary version of this work was presented at the ASME IDETC-CIE 2025 MSNDC Conference.

Availability of Data and Materials

The datasets generated and/or analyzed during the current study are available from the corresponding author on reasonable request.

References

1. Bae, J.S., Inman, D.J., Lee, I.: Effects of structural nonlinearity on subsonic aeroelastic characteristics of an aircraft wing with control surface. Journal of Fluids and Structures 19, 747-763 (2004)
2. Zhou, X., Huang, R.: Efficient nonlinear aeroelastic analysis of a morphing wing via parameterized fictitious mode method. Nonlinear Dyn. 105, 1-23 (2021)
3. Eller, D.: Friction, Freeplay and Flutter of Manually Controlled Aircraft. (2007)
4. Panchal, J., Benaroya, H.: Review of control surface freeplay. Progress in Aerospace Sciences 127, (2021)
5. Hernandez, S., Menga, E., Naveira, P., Lopez, C., Baldomir, A., Cid, M., Moledo, S., Freire, D.: Dynamic analysis of assembled aircraft structures with nonlinear joints. 58th AIAA/ASCE/AHS/ASC Structures, Structural Dynamics, and Materials Conference, (2017)
6. Ai, X., Bai, Y., Qian, W., Li, Y., Chen, X.: Aeroelastic investigation on an all-movable horizontal tail with free-play nonlinearity. Journal of Low Frequency Noise, Vibration and Active Control 43, 634-650 (2024)
7. Breitbach, E.: Effects of structural non-linearities on aircraft vibration and flutter. AGARD Reston, VA, USA, (1978)
8. Haidl, G.: Non-Linear Effects in Aircraft Ground and Flight Vibration Tests. (1976)
9. Shubov, M.A.: Flutter phenomenon in aeroelasticity and its mathematical analysis. Journal of Aerospace Engineering 19, 1-12 (2006)
10. Chen, P.C., Lee, D.H.: Flight-loads effects on free-play induced limit cycle oscillation. In: 47th AIAA/ASME/ASCE/AHS/ASC Structures, Structural Dynamics, and Materials Conference 14th AIAA/ASME/AHS Adaptive Structures Conference 7th, pp. 1851. (1851)
11. Conner, M.D., Tang, D., Dowell, E., Virgin, L.N.: Nonlinear behavior of a typical airfoil section with control surface freeplay: a numerical and experimental study. Journal of Fluids and structures 11, 89-109 (1997)
12. O'Neil, T., Strganac, T.W.: Aeroelastic response of a rigid wing supported by nonlinear springs. Journal of Aircraft 35, 616-622 (1998)

13. Riso, C., Cesnik, C.E.: Geometrically nonlinear effects in wing aeroelastic dynamics at large deflections. Journal of Fluids and Structures 120, 103897 (2023)
14. Emory, C.W., Patil, M.J.: Predicting limit cycle oscillation in an aeroelastic system using nonlinear normal modes. Journal of aircraft 50, 73-81 (2013)
15. Kuether, R.J., Allen, M.S.: A numerical approach to directly compute nonlinear normal modes of geometrically nonlinear finite element models. Mechanical Systems and Signal Processing 46, 1-15 (2014)
16. Peeters, M., Kerschen, G., Golinval, J.C., Stéphan, C., Lubrina, P.: Nonlinear Normal Modes of a Full-Scale Aircraft. Modal Analysis Topics, Volume 3, pp. 223-242 (2011)
17. Craig, R.R., Bampton, M.C.C.: Coupling of substructures for dynamic analyses. AIAA Journal 6, 1313-1319 (1968)
18. Peeters, M., Viguié, R., Sérandour, G., Kerschen, G., Golinval, J.C.: Nonlinear normal modes, Part II: Toward a practical computation using numerical continuation techniques. Mechanical Systems and Signal Processing 23, 195-216 (2009)
19. Huang, S.-C., Tien, M.-H.: A hybrid continuation framework for analyzing nonlinear normal modes of systems with contact nonlinearity. Journal of Computational and Nonlinear Dynamics 19, 071008 (2024)
20. Tien, M.-H., D'Souza, K.: Analyzing bilinear systems using a new hybrid symbolic-numeric computational method. Journal of Vibration and Acoustics 141, 031008 (2019)
21. Chen, X.-H., Tien, M.-H.: Method for Constructing a Compact Component Mode Synthesis Model for Analyzing Nonlinear Normal Modes of Structures With Localized Nonlinearities. Journal of Vibration and Acoustics 146, (2024)
22. Luber, W.G.: Limit Cycle Oscillation on Control Surfaces Due to Freeplay. In: NATO Science and Technology Organization Symposium, NATO RTO-MP-AVT-152-18. (2008)
23. Pereira, D.d.A., Vasconcellos, R.M.G.d., Marques, F.D.: Continuous function modelling to represent an airfoil control surface freeplay. Anais (2014)
24. Hinke, L., Dohnal, F., Mace, B.R., Waters, T.P., Ferguson, N.S.: Component mode synthesis as a framework for uncertainty analysis. Journal of Sound and Vibration 324, 161-178 (2009)
25. Tien, M.-H., D'Souza, K.: Transient dynamic analysis of cracked structures with multiple contact pairs using generalized HSNC. Nonlinear Dyn. 96, 1115-1131 (2019)
26. Osborne, M.R.: On shooting methods for boundary value problems. Journal of mathematical analysis and applications 27, 417-433 (1969)
27. Banerjee, B., Chen, J., Kathirgamanathan, A., Das, R.: Comparison of ANSYS elements SHELL181 and SOLSH190. Res. Rep., Univ. of Auckland, New Zealand 30 (2011)